Sodium and potassium ion storage in cation substituted 2D $MoWSe_2$: insights into the effects of upper voltage cut-off

To cite this article: Sonjoy Dey and Gurpreet Singh 2023 *Nanotechnology* **34** 385401

OPEN ACCESS
IOP Publishing
Nanotechnology
Nanotechnology **34** (2023) 385401 (13pp)
https://doi.org/10.1088/1361-6528/acdf66

Sodium and potassium ion storage in cation substituted 2D $MoWSe_2$: insights into the effects of upper voltage cut-off

Sonjoy Dey* and **Gurpreet Singh**

Department of Mechanical and Nuclear Engineering, Kansas State University, Manhattan, KS 66506, United States of America

E-mail: sonjoy@ksu.edu and gurpreet@ksu.edu

Received 6 April 2023, revised 8 June 2023
Accepted for publication 19 June 2023
Published 5 July 2023

Abstract

The superior properties, such as large interlayer spacing and the ability to host large alkali-metal ions, of two-dimensional (2D) materials based on transition metal di-chalcogenides (TMDs) enable next-generation battery development beyond lithium-ion rechargeable batteries. In addition, compelling but rarely inspected TMD alloys provide additional opportunities to tailor bandgap and enhance thermodynamic stability. This study explores the sodium-ion (Na-ion) and potassium-ion (K-ion) storage behavior of cation-substituted molybdenum tungsten diselenide ($MoWSe_2$), a TMD alloy. This research also investigates upper potential suspension to overcome obstacles commonly associated with TMD materials, such as capacity fading at high current rates, prolonged cycling conditions, and voltage polarization during conversion reaction. The voltage cut-off was restricted to 1.5 V, 2.0 V, and 2.5 V to realize the material's Na^+ and K^+ ion storage behavior. Three-dimensional (3D) surface plots of differential capacity analysis up to prolonged cycles revealed the convenience of voltage suspension as a viable method for structural preservation. Moreover, the cells with higher potential cut-off values conveyed improved cycling stability, higher and stable coulombic efficiency for Na^+ and K^+ ion half-cells, and increased capacity retention for Na^+ ion half-cells, respectively, with half-cells cycled at higher voltage ranges.

Supplementary material for this article is available online

Keywords: sodium ion batteries, potassium ion batteries, 2D materials, TMDs, TMD alloys, $MoWSe_2$

(Some figures may appear in colour only in the online journal)

1. Introduction

Investigations of transition metal di-chalcogenides (TMDs) that include MoS_2, $MoSe_2$, WS_2, and WSe_2 as electrodes in electrochemical energy storage devices have increased in recent years, encompassing practical research of traditional Li^+ ion-based rechargeable batteries and next-generation, Earth-abundant sodium-ion batteries (NIBs) and potassium-ion batteries (KIBs) [1–3]. However, TMD's inherent drawbacks (low electronic conductivity and severe volume change during electrochemical redox reaction) yield undesirable outcomes, such as menial reaction kinetics, capacity fading, and intense polarization that decreases energy inefficiency [4]. Strategies such as the interlayer expansion of lamellae to enhance the intercalation reaction [5, 6], improve reaction kinetics via conductive skeleton materials [7–9], and distinctive nanostructure formation to amplify rate capability and

* Author to whom any correspondence should be addressed.

cycling efficiency [10–12] have been widely investigated. However, these modification procedures usually require a complicated synthesis route with convoluted parameters. Nevertheless, several intercalating agents introduce impurities within the material, further sacrificing the conductivity of TMDs [13], while other utilized techniques induce regional atomic disorder and generate a 1 T phase [6, 14]. In addition, coupling with conductive materials such as graphene paper and carbon additives supplementally reduces energy density. Therefore, future research should include deterministic methodical strategies.

Doping and alloying have been shown to effectively tailor the intrinsic properties of TMDs, and a substitutional alloying strategy can engineer TMD bandgaps. For example, the substitution of anion and cation sites within MoS_2 to fabricate $Mo_xW_{1-x}S_2$, $MoS_{2x}Se_{2(1-x)}$ has resulted in a tuned bandgap of 1.8–2.0 eV and 1.6–1.9 eV, respectively [15, 16]. In addition, an informed choice of transition metal alloying potentially increases the thermodynamic stability of ordered materials with a wide bandgap tuning ability of approx. 1 eV [17]. Because TMD materials have many atomic species, the versatile chemistry of TMD alloys increases their potential for engineering nanoscale applications. Consequently, TMD alloys have already been utilized in a wide range of practical devices, such as water splitting [18], photovoltaics [19], and gas sensing [20].

Overall, current research regarding electrochemical energy storage devices has focused on the application of TMD alloys, but most of the research has highlighted their usage in Li^+ ion-based storage technologies [21–24], with only a few investigations of Earth-abundant, beyond lithium-ion (Li^+ ion)-based storage opportunities. For example, Mudgal *et al* investigated MoSeTe as an anode for NIBs, but the study only investigated up to 10 cycles. Furthermore, few studies have utilized anion-substituted TMD alloys, such as MoSSe, with carbon additives, such as N-doped carbon [25], rGO [26], and carbon nanotubes [27]. The aforementioned techniques potentially decrease the energy density in a full cell, thereby significantly affecting the charge transport due to variations in bonding and relative position of TMD and carbon [28]. Hanna *et al* created anion vacancies to investigate MoSSe in KIB storage applications by tediously optimizing the Se:S ratio during alloying to tailor particular properties [29]. Although a plethora of literature addresses anion-substituted TMD alloy for electrochemical energy storage devices, only a few investigations focus on cation-substituted TMD alloy and even less focus on NIBs and KIBs. For example, $MoWSe_2$ has been investigated as a potential LIB electrode, but the study considered using a three-electrode system, which exceeds the scope of practical application [30].

This report investigates the applicability of $MoWSe_2$, a cation-substituted TMD alloy, beyond Li^+ ion storage application, specifically the Na^+ and K^+ ion storage properties of the $MoWSe_2$ alloy and subsequent internal reactions. This study also investigated the promise of $MoWSe_2$ in Na-ion and K-ion half-cells by reducing the upper potential values to prevent structural distortion of the $MoWSe_2$ alloy. Although TMDs utilize both intercalation and conversion reactions during alkali-metal ion storage and their structural distortion occurs during prolonged cycling, previous studies have indicated that structural integrity preservation plays a decisive role in reaching the goal of stable capacity [31, 32]. The structural disintegration is even more prominent beyond Li-ion storage technologies as Na^+ and K^+ ions are bulkier in size and possess slower diffusion kinetics than Li^+ ions. For cation-substituted TMD alloys such as $MoWSe_2$, a comparatively higher conversion reaction rate was expected than the neat TMDs, potentially leading to severe structure pulverization, as proven by broadened peaks of the differential capacity curves for both $MoSe_2$ and WSe_2. Therefore, the upper potential suspension strategy was utilized to preserve the crystal structure within the material-restricting pulverization of the $MoWSe_2$ alloy to achieve stability during rate capability and the long-term cyclability test. The upper potential cut-off approach revealed that $MoWSe_2$ electrodes cycled in a range of 0.01–1.5 V, with approximately 29% higher capacity retention for Na^+ ion half-cells due to the restriction of specific reactions. Moreover, higher coulombic efficiency was observed, reaching near 100% for a half-cell cycle at 0.01–1.5 V. Therefore, the upper potential restriction could be vital for studying Na^+ and K^+ ion storage in TMD alloys to improve cycling stability.

2. Materials, methods, and characterization

2.1. Morphologic and spectroscopic characterization

This study carried out transmission electron microscopy (TEM) and energy-dispersive x-ray spectroscopy on an FEI Tecnai Osiris 200 kV. Selected area electron diffraction (SAED) image was obtained using Phillips CM100 TEM. Raman spectrum of the sample utilized a LabRAM ARAMIS Jobin Yvon Raman spectrometer with a HeNe laser ($\lambda = 633$ nm) as an excitation source. X-ray photoelectron spectroscopy (XPS) data were obtained using a thermo scientific equipped with a monochromatic Al anode Kα ($h\nu = 1486.6$ eV) with *in situ* sputtering of Ar^+ at 3.0 keV for 120 s. Scanning electron microscopy (SEM) images of the disassembled cells were collected using Hitachi SU8010. The IXRF system obtained the corresponding x-ray fluorescence (XRF) spectrum.

2.2. Electrochemical characterization

The preparation of electrodes included 70 wt% of $MoWSe_2$ powder as received (Ossila, 99.9%), 15 wt% of carbon black (Alfa Aesar, 99.9%), and 15 wt% poly(vinylidene fluoride) (Alfa Aesar) mixed with a few drops of 1-Methyl-2-pyrrolidinone (Sigma Aldrich) until a homogenous slurry was achieved. The obtained slurry was coated onto a copper foil with a thickness of 9 μm and dried at 80 °C overnight. The obtained coating on the copper foil (125 μm thick) was cut into circular sections with diameters of 14.29 mm, which were used as working electrodes in Na^+ ion and K^+ ion half-cells, where the counter electrodes were Na and K metal,

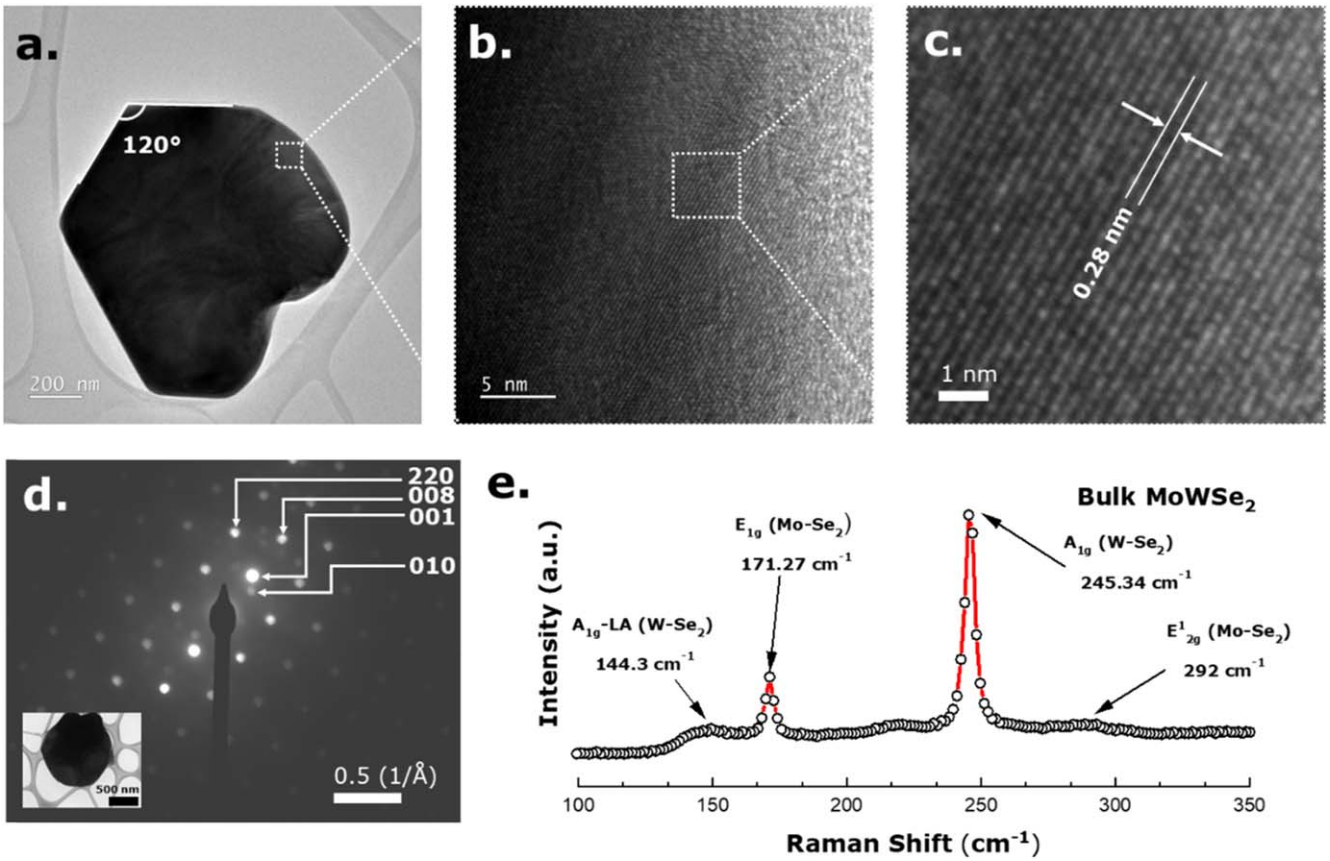

Figure 1. (a) Low-resolution TEM images of the $MoWSe_2$ flakes; (b), (c) high-resolution TEM images of $MoWSe_2$ nanosheets; (d) six-fold symmetrical SAED spot pattern generated from the $MoWSe_2$ bulk flake shown in the index; (e) Raman spectrum of bulk $MoWSe_2$ alloy depicting different vibrational modes.

respectively. The electrolytes for Na^+ ion and K^+ ion half-cells were 1.0 M $NaClO_4$ (Alfa Aesar) in (1:1 v/v) Ethylene Carbonate (EC): Dimethyl Carbonate (DMC) (anhydrous, 99% Sigma Aldrich) and 1.0 M KPF_6 (Alfa Aesar) in (1:1 v/v) EC: DMC, respectively. All the half-cell assemblies utilized a high-precision argon atmosphere with O_2 and H_2O contents below 0.1 ppm. An Arbin BT 2000 test unit was used to investigate the electrochemical behavior of the assembled CR-2023 coin cells under potential ranges of 0.01–1.5 V, 0.01–2.0 V, and 0.01–2.5 V. A rate capability test was done under asymmetric cycling, in which sodiation and potassiation were carried out in 100 mA g^{-1} current density, and desodiation and depotassiation were carried out with stepwise increase and varying current densities. In addition, the cycling stability of electrodes was investigated under symmetric cycling conditions of 100 mA g^{-1} current density.

3. Results and discussion

3.1. Microscopic and spectroscopic analysis

Figure 1(a) shows the low-resolution TEM micrograph of the $MoWSe_2$ sheets with a 120° edge angle, which is typical for TMD nanosheets. Figures 1(b) and (c) further illustrate the sheet-like stacked structure of the $MoWSe_2$, confirming the existence of the bulk sheets. The fringes observed in figure 1(c) were further analyzed to investigate the distance between them. Specifically, the fast Fourier transform (FFT) of figure 1(c), inverse FFT from the brightest spot, and finally, the fringe intensity profile (figures S1(a)–S1(c), respectively) were analyzed. The inter-fringe distance was found to be approx. 0.28 nm—in agreement with the interlayer lattice spacing value regarding (100) and (101) planes of hexagonal $MoSe_2$ and WSe_2 [33]. Figure 1(d) shows the SAED pattern of bulk $MoWSe_2$ powder. TEM micrograph on the inset of figure 1(d) shows the flake from where the SAED was obtained. Specifically, the six-fold symmetrical spot pattern reflection from the SAED indicates the polycrystalline nature of the $MoWSe_2$ flake. Individual spots were assigned to the combination of (010), (220) planes of $MoSe_2$ [34, 35] and (001), (008) planes of WSe_2 material [36].

Raman spectroscopy was used to characterize the bulk $MoWSe_2$ powder to confirm the presence of both Mo and W species bonded with Se. In addition, Raman spectra of the bulk $MoSe_2$ and WSe_2 powders were obtained and analyzed for comparison with bulk $MoWSe_2$ powder. The detailed analysis of the bands originating from the Raman spectra of $MoSe_2$ and WSe_2 bulk powders is provided in the supplementary information figures S2(a)–(c). Figure S2(c) shows

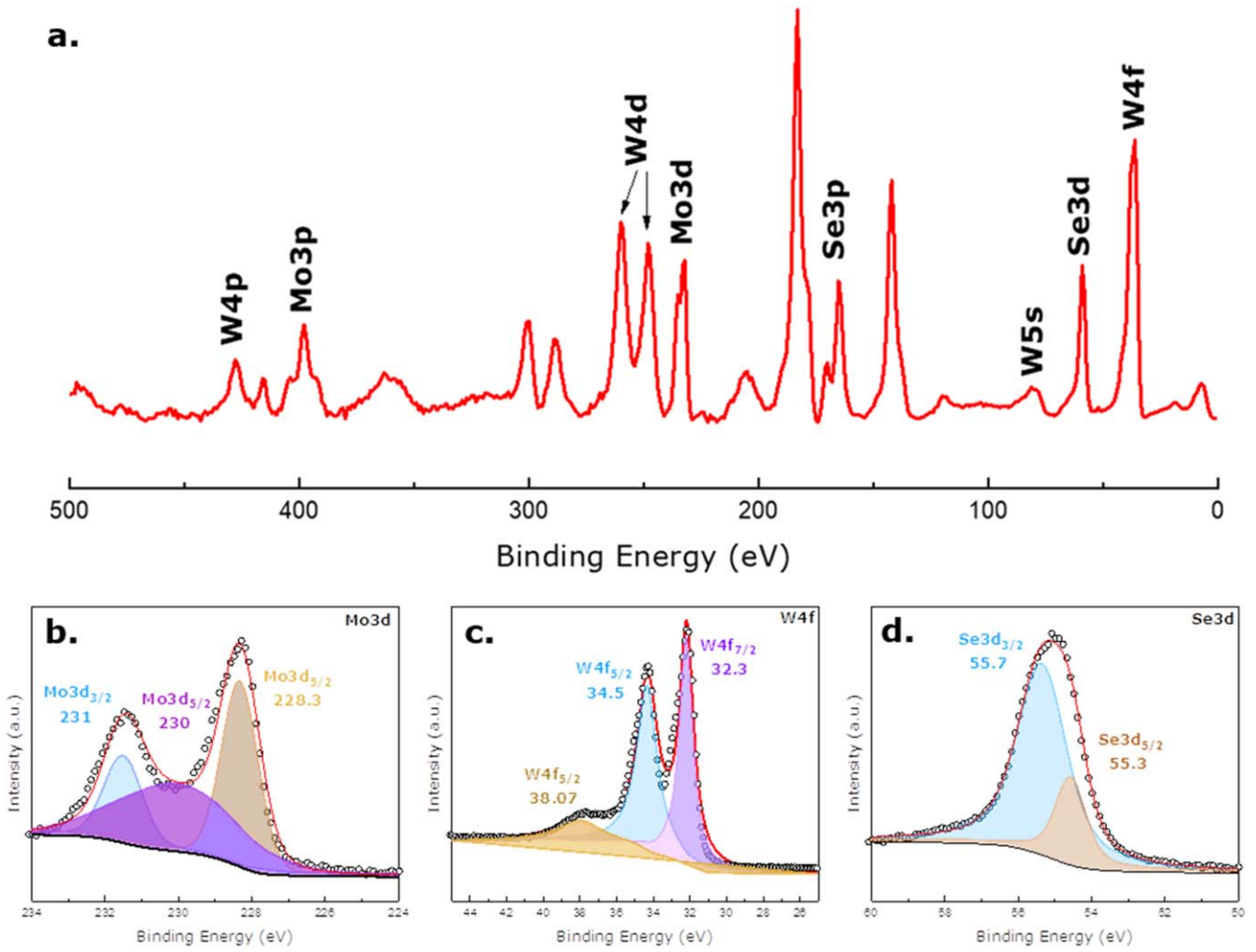

Figure 2. (a) XPS survey scan depicting the presence of different materials within $MoWSe_2$; high-resolution (b) Mo 3d; (c) W 4f; (d) Se 3d XPS spectra of the $MoWSe_2$ material illustrating the chemical bonding states.

the schematic of various vibration modes originating from typical TMD materials. The A_{1g} vibration mode arises from the out-of-plane relative motion of the Se atoms concerning the Mo/W atom being stationary. In contrast, the E^1_{2g} vibration mode dictates the in-plane opposing vibration of Mo/W and Se atoms, and the E_{1g} mode defines the in-plane relative vibrational motion of the chalcogen atoms (Se) [37].

The as-obtained Raman spectrum of $MoWSe_2$ powder is illustrated in figure 1(e), which shows the intense and prominent out-of-plane A_{1g} mode of Mo bonded with Se [38]. For the $MoWSe_2$ alloy, the A_{1g} mode shifted from 240.1 to 249.3 cm^{-1}, depending on the composition of W ranging from 0 to 1 in $Mo_{1-x}W_xSe_2$. This shift in A_{1g} mode originating due to linear dependence of W atoms indicates that the examined sample typically possesses $x = 0.5$ fraction—further indicating that the Mo : W ratio was 1:1 in the bulk material [39]. Noticeably, this peak may look broader due to the proximity of the A_{1g} and E^1_{2g} modes of WSe_2 [40]. Peaks at 171.27 cm^{-1} and 292 cm^{-1} were also observed due to the E_{1g} and E^1_{2g} modes of $MoSe_2$, respectively [41, 42]. Additionally, one weaker peak at 144.3 cm^{-1} originated from the A_{1g}-LA (longitudinal acoustic) mode of WSe_2 due to single degenerate vibrations of the lattice [43]. Modes such as $E_{1g} + A_{1g}$, $E^1_{2g} + LA(M)$, and $E^1_{2g} + E_{1g}$, which are typically observed in monolayer and bilayer materials, were noticeably absent in the bulk $MoWSe_2$ with the Mo and W ratio of 1:1 [39]. Moreover, in the bulk material, the B^1_{2g} mode was not visible for being Raman inactive, typically originating due to increased symmetry in the monolayer or bilayer materials [44, 45].

Figure 2(a) shows the XPS survey scan of the $MoWSe_2$ powder, and figures 2(b)–(d) present high-resolution scans of the Mo 3d, W 4f, and Se 3d spectra, respectively. In addition to the desired Mo, W, and Se elements, other peaks were observed in the survey scan due to the sample preparation process. The atomic wt% of the elements in the sample, specifically Mo (7.96), W (10.61), and Se (26.57) maintain close to a 1:1:2 stoichiometric ratio. The deconvolution of Mo 3d high-resolution spectra in figure 2(b) shows three distinct peaks: the Mo $3d_{3/2}$ peak in the 231 eV region due to elemental Mo species [46] (possibly due to the sputtering process before XPS measurement) and two Mo $3d_{5/2}$ peaks in the

230 eV and 228.3 eV regions, indicating the oxidized Mo species [47] (due to the sample preparation process) and Mo bonded with Se, respectively [48]. The peak-fitted W 4f spectra revealed three peaks at 38.07 eV, 34.5 eV, and 32.3 eV (figure 2(c)), with the first peak being the W $4f_{5/2}$ peak from the oxidized WO_x/W species [49] and the W $4f_{5/2}$ and W $4f_{7/2}$ peaks from the WSe_2 species [50], respectively. Finally, the deconvoluted Se 3d spectra (figure 2(d)) show two Se $3d_{3/2}$ peaks at 55.7 eV and 55.3 eV, with the former from the di-selenide moiety of $MoSe_2$ [51] and the latter from the WSe_2 [52].

3.2. Electrochemistry

3.2.1. Na^+ ion storage. This study investigated Na^+ ion electrochemical reactions during sodiation/desodiation in the $MoWSe_2$ electrode using characteristic galvanostatic charge–discharge curves. The derived differential capacity curves from the charge–discharge curves provided the plateau regions of the charge–discharge curves as specific peaks at 100 mA g^{-1}. Figure 3(a) illustrates the sodiation/desodiation within the potential range of 0.01–2.5 V. As shown in the derived differential capacity curve in supplementary figure S3(a), several peaks indicate a mixture of reactions with $MoSe_2$ and WSe_2 within the TMD alloy ($MoWSe_2$) during the first-cycle sodiation. The first-cycle sodiation curve has major peaks at 0.59 V, 0.53 V, 0.16 V, and 0.01 V, possibly due to the Na/Se conversion reaction and the formation of the irreversible solid electrolyte layer (SEI) (0.01 V), as shown in figure S3(a) with an intense peak only in the first cycle. Previous studies ascribed peaks near the approx. 0.5 V region to the irreversible conversion reaction of $MoSe_2$, and peaks <0.25 V were ascribed to the conversion reaction from the WSe_2 conversion product [53–55].

Although both reactions of the $MoWSe_2$ electrode appeared in the first-cycle sodiation curves, peaks in the 1.48 V and 1.87 V regions began to appear in the second cycle due to possible intercalation of Na^+ ions into the layers of $MoWSe_2$, as visible up to the 50th cycle (figures 3(b) and S3(a)). As mentioned, the peak intensity decreased from the first to the 50th cycle, potentially indicating fewer sites of $MoWSe_2$ to facilitate the gradual intercalation of Na^+ ions. A notable peak shift of the 1.48 V and 1.87 V reactions was observable in subsequent cycles to lower potential values, as shown in the surface plot (figure 3(b)) and the 2D plot (figure S3(a)). The shift for the 1.48 V peak was 0.03 V, while the observed shift for the 1.87 V peak was 0.06 V for the 0.01–2.5 V electrode (figure S3(a)). Noticeable peaks were observed at 0.1 V, 1.73 V, and 2.1 V (figure S3(a)) in the first-cycle desodiation curve, of which the 1.73 V and 2.1 V peaks may be due to the reverse conversion and intercalation reactions, respectively. Previous literature has attributed the approx. 1.7 V peak to the extraction of Na^+ ions from WSe_2 electrodes or the reverse conversion reaction, but the 2.1 V is due to the reverse Na–Se reaction or the reverse intercalation reaction [56]. Although a shift of 0.04 V was observed for the 1.73 V peak up to the fifth cycle, the 2.1 V peak showed no such phenomenon (figure S3(a)). Previous studies have suggested that the shift of peak locations to higher potential values during charge and lower potential values during discharge are due to resistive and diffusive polarization effects [57]. Because a lower voltage shift of peaks was discerned for the intercalation reaction, the conversion reaction may cause the most polarization effect. Moreover, the three-dimensional (3D) differential capacity curves of the desodiation cycle in figure 3(c) show that the 0.1 V peak continues up to 140th cycle with slight polarization from the 100th cycle. In addition, the surface plot shows that the 2.1 V and the 1.73 V merge into one 1.73 V peak up to the 75th cycle and then eventually decrease in intensity, indicating a permanent structural change after the specific cycle.

The $MoWSe_2$ electrode was cycled within the potential range of 0.01–2.0 V in similar conditions. The characteristic differential capacity curve (figure S3(b)) derived from the galvanostatic charge–discharge curve (figure 3(d)) of the half-cell showed the same peaks, indicating no unique reactions due to upper voltage cut-off values. For the 0.01–2.0 V cell, several peaks typically due to conversion and intercalation reactions appeared at 1.25–2.0 V, with the center peak at 1.73 V (figure 3(e)). The 1.73 V peak was visible up to the 90th cycle, as shown in the surface plot (figure 3(e)) with a green peaked contour profile, comparatively better than the 0.1–2.5 V cell, indicating the advantage of upper voltage suspension for structural stability. Although the peak shift of the desodiation curve (figure 3(f)) showed values similar to the 0.01–2.5 V cell, higher values of the shift were observed for the peak at 1.73 V, indicating a change in 0.06 V up to five cycles.

When the $MoWSe_2$ electrode was cycled in the potential range of 0.01–1.5 V (figure 3(g)), the derived differential capacity curve (figure S3(c)) showed no prominent peaks except the conversion reaction peaks of the first-cycle desodiation, indicating that voltage restriction prevents most of the redox reaction. However, a low intense peak was observed in the 1.5 V region in the desodiation curve, potentially due to a partial intercalation reaction at a lower voltage that does not fade away until the 50th cycle. Although the peaks in the sodiation (figure 3(h)) and desodiation (figure 3(i)) curves originating from the cell cycled at 0.01–1.5 V range were less intense than the other two cells cycled within different potential ranges, they were apparent up to the 140th cycle with consistent height (yellow for the sodiation curve and red for the desodiation curve in figures 3(h) and (i), respectively), indicating possible structure retention in harsh and prolonged cycling. Furthermore, the conversion reactions (<0.7 V region in green in the 3D surface plot in figure 3(h)) inside the material were also visible up to the 140th cycle, with high intensity (shown in red in figure 3(i)) for the first 20 cycles and lower intensity (shown in green in figure 3(i)) for the remaining 120 cycles.

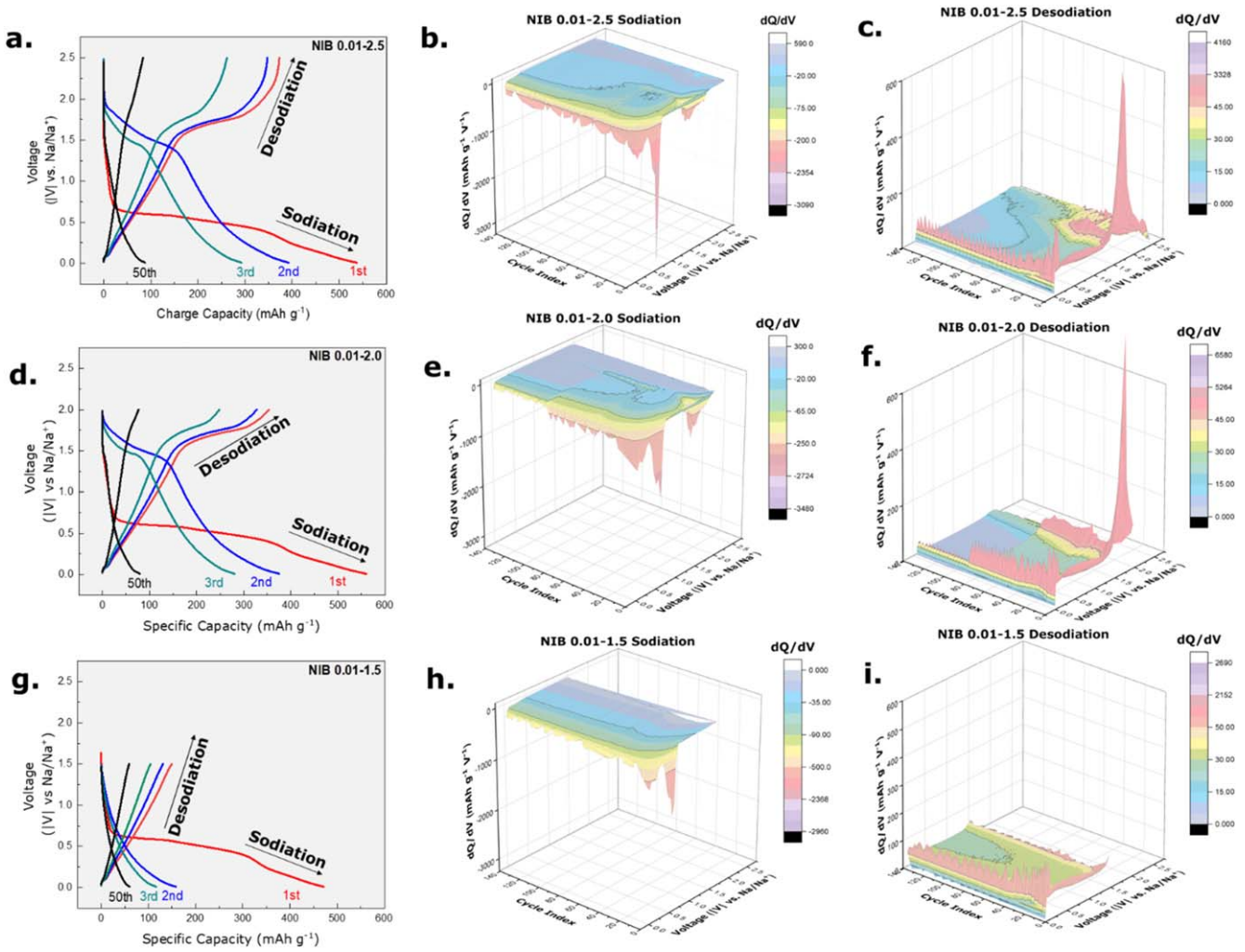

Figure 3. Investigation of Na^+ ion storage behavior: (a) Galvanostatic charge–discharge curves of $MoWSe_2$ electrode cycled within 0.01–2.5 V; differential capacity curves of (b) 1st–140th sodiation cycles, (c) 1st–140th desodiation cycles of 0.01–2.5 V $MoWSe_2$ electrode; (d) Galvanostatic charge–discharge curves of $MoWSe_2$ electrode cycled within 0.01–2.0 V; differential capacity curves of (e) 1st–140th sodiation cycles, (f) 1st–140th desodiation cycles of 0.01–2.0 V $MoWSe_2$ electrode; (g) Galvanostatic charge–discharge curves of $MoWSe_2$ electrode cycled within 0.01–1.5 V; differential capacity curves of (h) 1st–140th sodiation cycles, (i) 1st–140th desodiation cycles of 0.01–1.5 V $MoWSe_2$ electrode.

The performances of the three electrodes at different voltage ranges were tested in gradually increasing current densities of 100, 200, 400, 600, and 800 mA g^{-1} for five cycles and then returned to original current densities, as shown in figure 4(a). Both the 0.01–2.5 V and 0.01–2.0 V cells showed higher charge capacity (353 mAh g^{-1} and 372 mAh g^{-1}, respectively) than the 0.01–1.5 V cycled cell (149 mAh g^{-1}) in the initial cycles, but as shown in figure 4(a), in higher current densities, the 0.01–2.5 V cycled cell and the 0.01–2.0 V cycled cell showed gradual capacity fading. Less capacity fading was observed in the 0.01–1.5 V cycled cell. In the 5th, 10th, 15th, 20th, and 25th cycles, the 0.01–1.5 V cell showed 70%, 86%, 91%, 93%, and 95% capacity retention, respectively, constantly approx. 20%–30% higher than the other two electrodes, indirectly suggesting that the upper cut-off voltage significantly restricts capacity fading, leading to increased capacity retention and decreased structural distortion of the $MoWSe_2$ material. Following the rate capability test, the same cells were cycled at 100 mA g^{-1} current density for 100 cycles. As illustrated in figure 4(a), the capacity of the 0.01–2.5 V, and 0.01–2.0 V cells almost overlapped with the 0.01–1.5 V cell showed robust capacity up to the 140th cycle. In order to further emphasize the merits of voltage cut-off technique, three additional cells were assembled and cycled at 100 mA g^{-1}, for performace evaluation at fixed cycling current. All three cells displayed low coulombic efficiency at the initial cycle, possibly due to the side reactions from electrolyte reduction in the initial cycle [58].

Figure 4(a) also shows that the high coulombic efficiency of the 0.01–1.5 V cycled cell exceeded 90% during the rate capability test at the seventh cycle for the Na^+ ion half-cell, while the coulombic efficiency was 4%–5% lower for the other two cells. A similar trend of coulombic efficiency was observed for the newly assembled cells cycled at three potential ranges during the stability test (figure S4). In such conditions, the merit of upper voltage cut-off experiment was more apparent as the 0.01–2.5 V cell showed the most capacity degradation (starting from second cycle onwards),

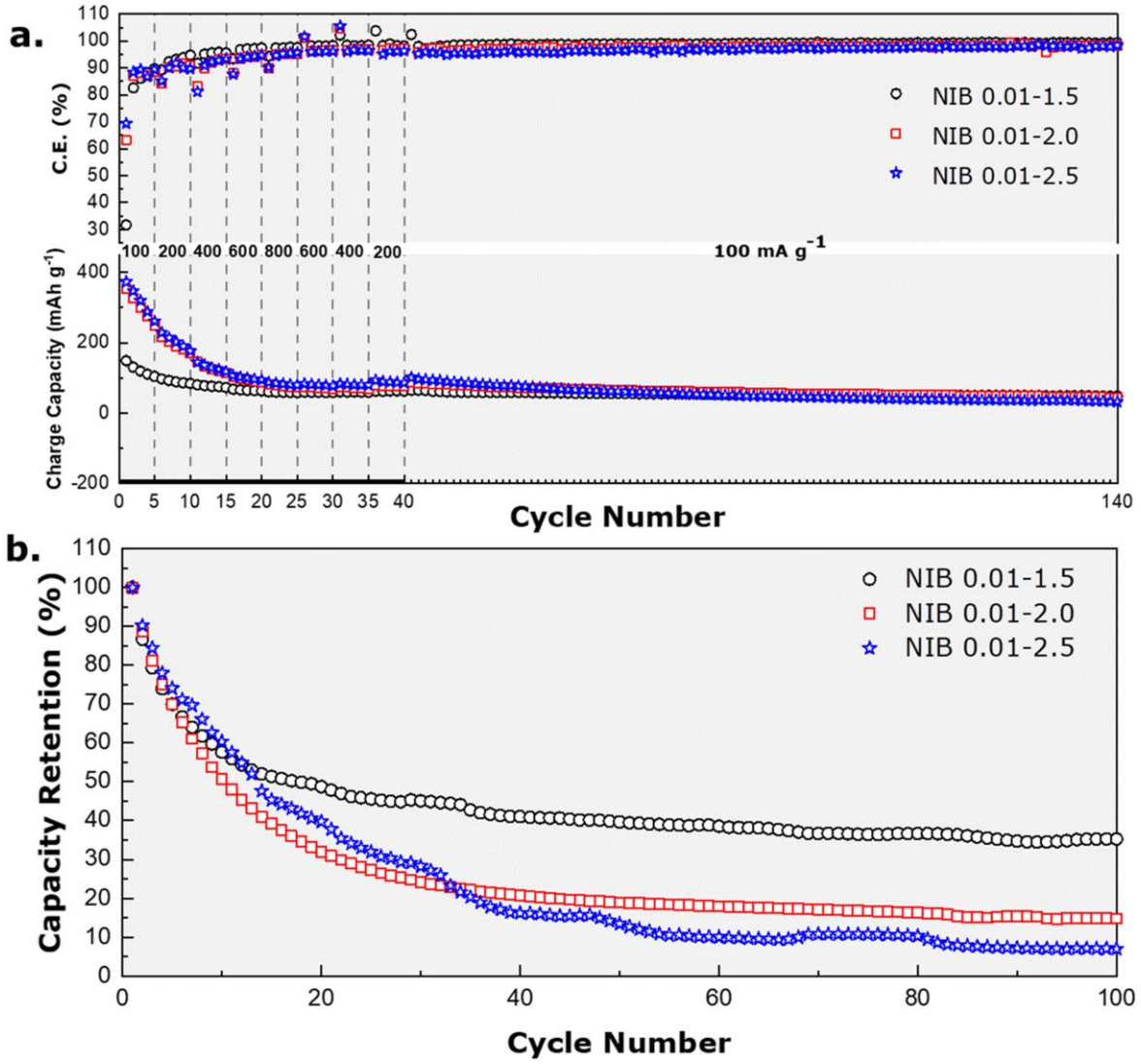

Figure 4. (a) Rate capability and consecutive cycling stability tests for investigating Na^+ ion storage behavior of half-cells cycled within different potential ranges; (b) capacity retention (%) during Na^+ ion storage of different half-cells cycled at various potential ranges throughout cycling stability test derived from figure S4.

while the 0.01–1.5 V was relatively stable. Figure 4(b) shows capacity retention (derived from figure S4) during the prolonged cycling period, where the cells with lower cut-off values (0.01–2.5 V) degrade fast—reaching 6.98% capacity retention in the 100th cycle. On the other hand in the 100th cycle, the capacity retention of the 0.01–1.5 V cell was 16% and 29% higher than the 0.01–2.0 V cell and 0.01–2.5 V cell, respectively, highlighting the benefits of the upper voltage cut-off for stable cycling conditions. Noticeably, capacity fading was also observed in case of the 0.01–1.5 V cell till the 14th cycle.

3.2.2. K^+ ion storage. K^+ ion storage behavior within the $MoWSe_2$ electrodes was investigated similarly. The differential capacity curve (figure S5(a)) derived from the charge–discharge curve (figure 5(a)) of the $MoWSe_2$ electrode cycled within the potential range 0.01–2.5 V indicated a combined reaction of $MoSe_2$ and WSe_2 material. Noticeably in figure 5(a), two prominent voltage plateaus were observed for KIB cells, while in NIB cells, one prominent plateau existed. The differential capacity curves further highlight the assignment of such plateaus. As shown in figure S5(a), the first cycle potassiation differential capacity curve reveals four prominent peaks and broad features below the 1 V region. These four peaks, which occur at 0.19 V, 0.36 V, 0.4 V, and 0.79 V and then disappear in subsequent cycles, were likely due to the irreversible conversion reaction associated with structural change and SEI layer formation. The peak at 0.79 V was attributed to K^+ ions interacting with $MoSe_2$ within the $MoWSe_2$ alloy [3]. In comparison, the broadening of the peak at 0.36–0.5 V was correlated with the K^+ ion interaction with the WSe_2 layer of the $MoWSe_2$ alloy. The peak at 0.17 V was ascribed to an irreversible conversion reaction of WSe_2 regions within the $MoWSe_2$ alloy and the formation of the SEI layer [59, 60]. Therefore, all the metals were assumed to participate in different electrochemical reactions with K^+ ions. After the first-cycle reactions, one peak at 1.24 V appeared from the second cycle onwards

primarily due to the reduction of Se from the $MoWSe_2$ to K_2Se (figure S5(a)), otherwise known as the reduction of metal selenide particles to form ultrafine crystals [61]. However, this peak shifted 0.05 V from the last place in the fifth cycle, potentially leading to polarization (figure S5(a)). The peak at 0.79 V continued until 0–20 and 40–60 cycles with decreasing intensity (shown in blue in figure 5(b)), thereby skipping the harsh current rates. Similar behavior was observed in the 1.24 V peak, in which a broad peak from 1.3 to 2.0 V was observed in the first to the fifth depotassiation cycle (figure S5(a)), with a prominence at 1.59 V in the first cycle, indicating a multistep reaction. Previous studies have identified peaks at 1.68 V and 2.06 V as phase transformations of K_2Se to K_2Se_n and Se [60], and the high voltage 1.73 V peak has been associated with the oxidation reaction of metallic Mo to reform $MoSe_2$ [62]. The prominent 1.73 V peak showed a shift of 0.02 V up to five cycles (figure S5(a)), and peaks at 1.3–2.0 V became less prominent as the cycling continued, partially disappearing midway during high current density cycling (shown in blue in figure 5(c)), losing their prominence in the 90th cycle (red to yellow on figure 5(c)), and continuing as a single, less intense peak up to the 140th cycle, as shown in figure 5(c). The 0.36 V peak showed polarization behavior moving up to 0.5 V at the end of the cycling.

For the half-cell cycled in the 0.01–2.0 V potential range (charge–discharge curve of figure 5(d) transformed into the differential capacity curve in figure S5(b)), all the same reactions as 0.01–2.5 V cell occurred since no other reactions were observed, thereby confirming the logic of restricting the potential range to 2.0 V for K^+ ion storage. A similar behavior was observed in the potassiation cycle (figure 5(e)) for the 0.01–2.0 V cell compared to the 0.01–2.5 V cell (figure 5(b)), where, for the depotassiation cycle, the 3D differential capacity curve in figure 5(f) shows that the 0.36 V curve maintains its intensity to the 140th cycle while

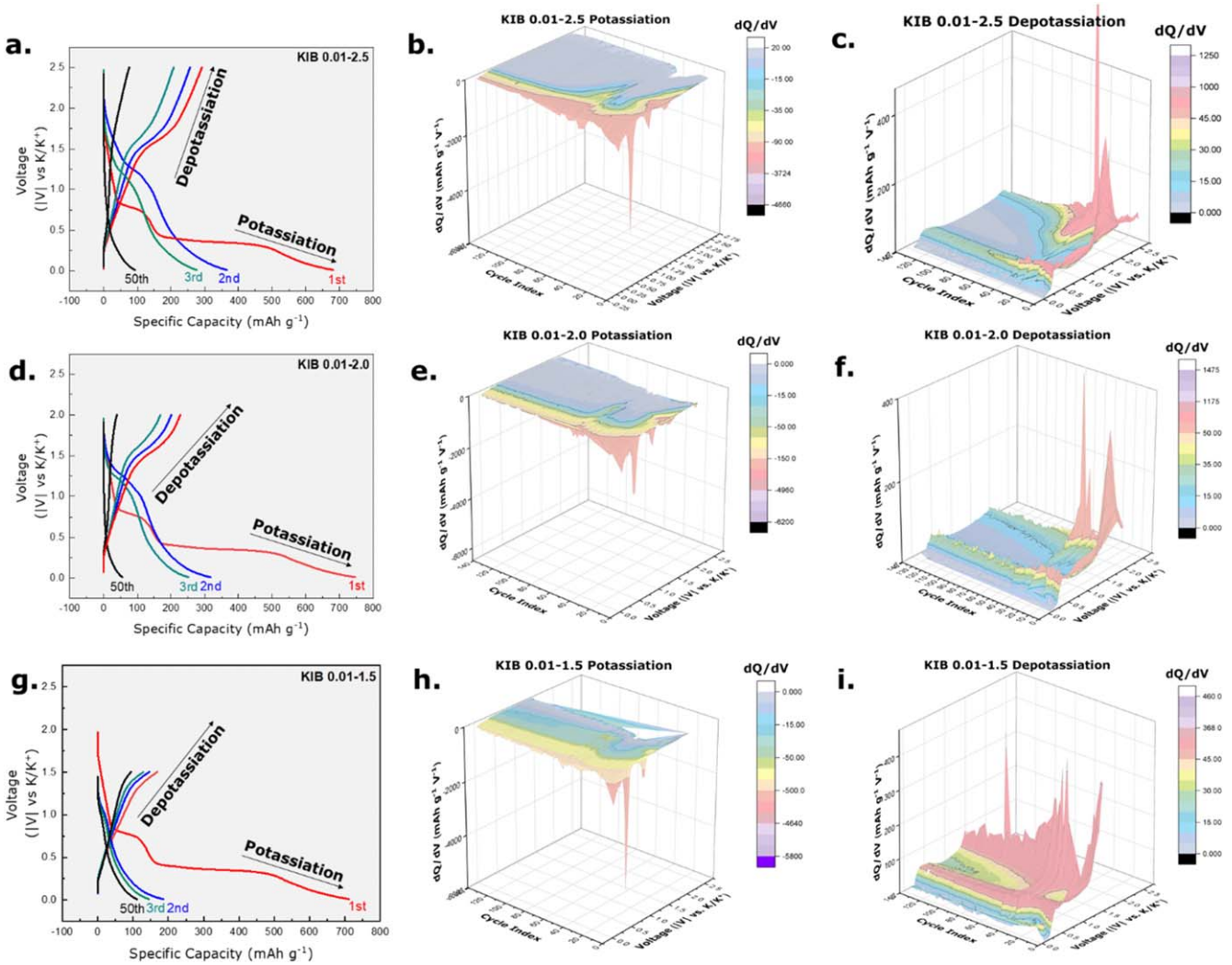

Figure 5. Investigation of K^+ ion storage behavior: (a) Galvanostatic charge–discharge curves of $MoWSe_2$ electrode cycled within 0.01–2.5 V; differential capacity curves of (b) 1st–140th potassiation cycles, (c) 1st–140th depotassiation cycles of 0.01–2.5 V $MoWSe_2$ electrode; (d) Galvanostatic charge–discharge curves of $MoWSe_2$ electrode cycled within 0.01–2.0 V; differential capacity curves of (e) 1st–140th potassiation cycles, (f) 1st–140th depotassiation cycles of 0.01–2.0 V $MoWSe_2$ electrode; (g) Galvanostatic charge–discharge curves of $MoWSe_2$ electrode cycled within 0.01–1.5 V; differential capacity curves of (h) 1st–140th potassiation cycles, (i) 1st–140th depotassiation cycles of 0.01–1.5 V $MoWSe_2$ electrode.

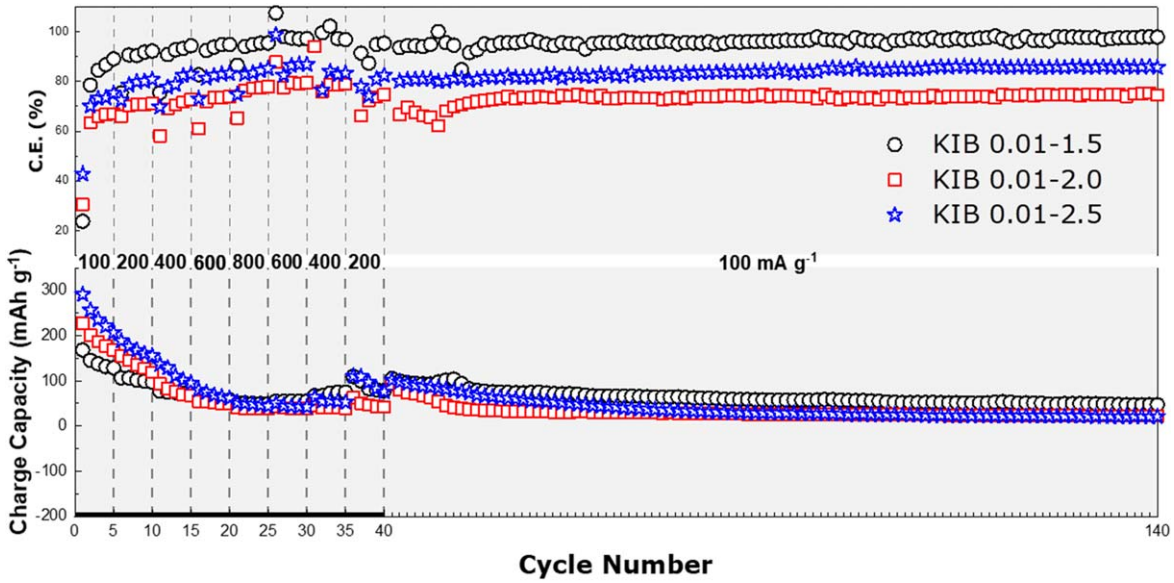

Figure 6. Rate capability and consecutive cycling stability tests for investigating K^+ ion storage behavior of half-cells cycled within different potential ranges.

undergoing a slight voltage shift and reaching 0.5 V. Although the peaks at the 1.3–2.0 V region survived the harsh cycling conditions, shown by the reactions up to the 140th cycle in figure 5(f) which highlights the benefit of upper voltage suspension, the peaks narrow in size at 1.6–2.0 V in the last cycles.

For the cell cycled in the potential range of 0.01–1.5 V (figure 5(g)), the potassiation differential capacity curve presented the conversion reactions in the first cycle. The potassiation curve for cycles 2–140 contained only one peak at 1.06 V and then gradually became less intense, indicating the possible continuation of the intercalation reaction and subsequent preservation of the crystal structure (figure 5(h)). In the depotassiation curve (figure 5(i)), the peak at 1.5 V occurred until the 140th cycle, indirectly proving that upper voltage suspension leads to longer reaction preservation in TMD alloys. The 0.36 V depotassiation peak also maintained uniform intensity throughout the harsh and prolonged cycling, showing hysteresis behavior during cycling at high current densities in which the peak moved to 0.5 V at the highest current density of 800 mA g^{-1}, implying that hysteresis may also increase at higher current densities (figure 5(i)).

The performances of the three electrodes were tested at different voltage ranges in gradually increasing and decreasing current densities of 100, 200, 400, 600 and 800 mA g^{-1} for five cycles up to the 25th cycle and then returned to the original current densities, as shown in figure 6. In the initial five cycles, both the 0.01–2.5 V and 0.01–2.0 V cells showed higher charge capacity (291 mAh g^{-1} and 227 mAh g^{-1}, respectively) than the 0.01–1.5 V cycled cell (168 mAh g^{-1}). However, as shown in figure 6, in higher current densities, the 0.01–2.5 V cycled cell and the 0.01–2.0 V cycled cell showed gradual capacity fading. In comparison, less capacity fading was observed in the 0.01–1.5 V cycled cell. In cycles 26, 31, 36, and 41 the cell cycled up to 1.5 V showed 76%, 91%, 93%, and 95% capacity retention, respectively, consistently approx. 10%–20% higher than the other two electrodes, suggesting that upper cut-off voltage restricts capacity fading. Higher voltage cut-off values may also decrease structural distortion of the $MoWSe_2$ material for K^+ ion storage.

After the rate capability test, the cells were cycled at 100 mA g^{-1} current density for additional 100 cycles. As illustrated in figure 6, although the charge capacity of 0.01–2.5 V and 0.01–2.0 V cells overlapped, the 0.01–1.5 V cell showed stable and slightly higher charge capacity. However, the benefits of upper voltage restriction were more apparent in coulombic efficiency chart, where the 0.01–1.5 V cell demonstrated high cycling efficiency (near 100%) during stability test after the rate capability. In contrast, the 0.1–2.0 V cell constantly showed much lower (approx. 80%) coulombic efficiency during rate capability and consequent stability test, while the coulombic efficiency of the 0.01–2.5 V cell was the lowest at approx. 70% (figure 6). This can be correlated with possible electrolyte consumption and structural degradation of the cells cycled at lower cut-off voltages.

4. Post-cycling analysis

To investigate the possible reasons for capacity fading of cells cycled at certain voltage range and consecutive higher capacity gain of cells cycled at higher cut-off voltages, selective spent cells were disassembled in an inert atmosphere, washed with DMC solvent for separator fiber and electrolyte contaminant desolvation. Digital camera images of electrodes cycled in 0.01–1.5 V and 0.01–2.5 V range are shown in figures S6(a)–(d). The recovered electrodes for the 0.01–2.5 V range (figures S6(a), (b) showed signs of significant damage. This damage can be correlated to the substantial volume change experienced by traditional TMD during alkali-metal ion accommodation, conversion reactions, and subsequent loss of adhesion (peel-off) of active materials from the current

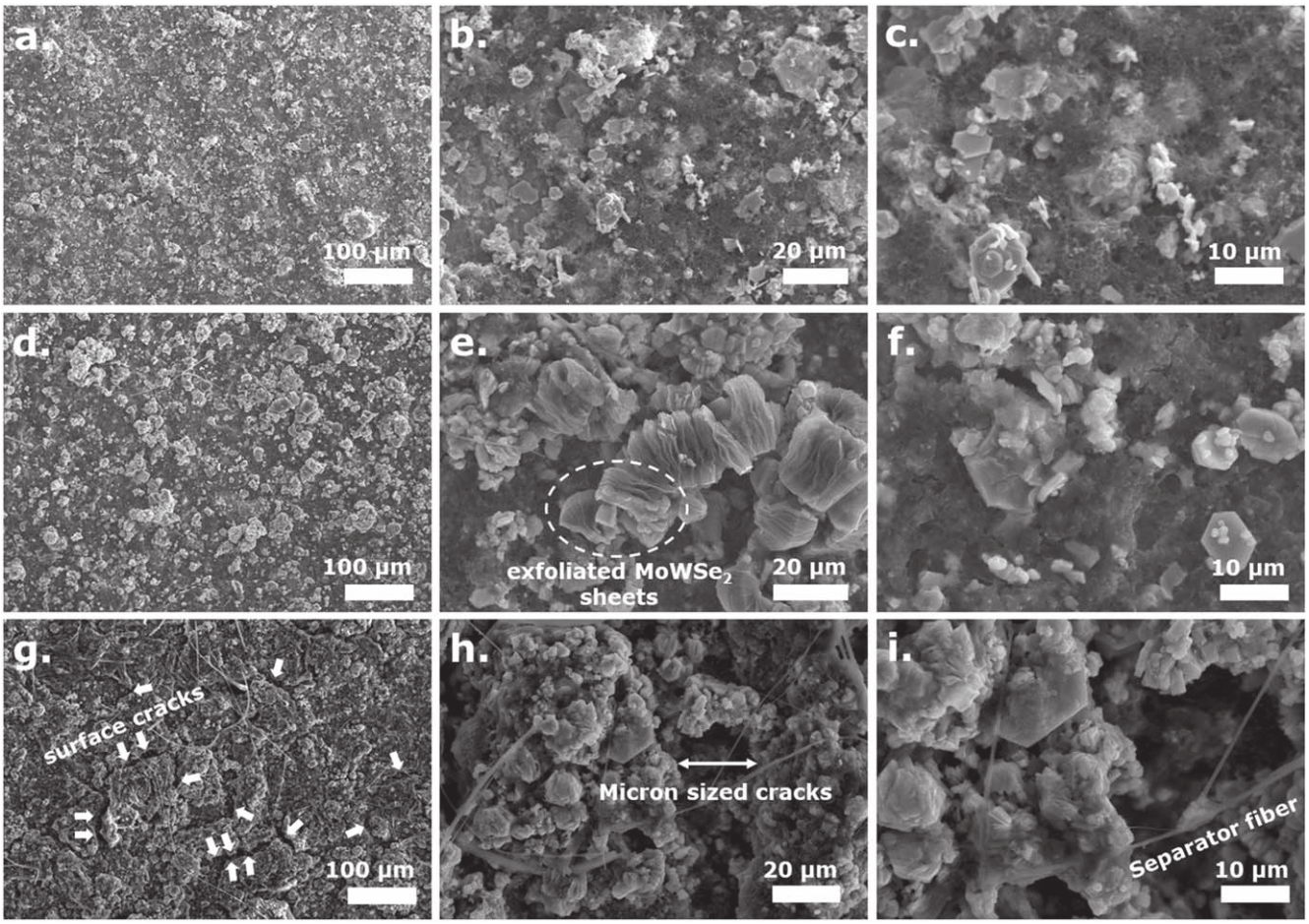

Figure 7. SEM micrographs of (a)–(c) Neat $MoWSe_2$ electrode showing smooth surface with $MoWSe_2$ sheet dispersion; (d)–(f) disassembled $MoWSe_2$ Na^+ ion half-cell electrode cycled within 0.01–1.5 V showing exfoliated flakes; (g)–(i) disassembled $MoWSe_2$ K^+ ion half-cell electrode cycled within 0.01–1.5 V showing microcracks generated due to cycling.

collector [63–65]. Hence, SEM analysis of such electrodes was avoided.

On the other hand, the electrodes cycled in the 0.01–1.5 V range experienced significantly less damage (figures S6(c), (d))—the active material was still retained on the copper current collector. The above electrodes were further analyzed using SEM and XRF (elemental analysis) and compared with the uncycled $MoWSe_2$ electrode. As can be seen in figures 7(a)–(c), the neat electrodes possessed smooth geometrical features with somewhat homogeneous dispersion of micron-size $MoWSe_2$ particles. The XRF spectra of the electrode (figure S7(a)) showed the presence of Mo, W, Se, and C (originating from the binder and conductive agent particles) elements. The SEM micrograph (figure 7(d)) of the disassembled electrode, cycled in the 0.01–1.5 V (v/s Na^+) range, shows a relatively smooth surface geometry similar to the uncycled electrode. Insertion of Na^+ ions into the $MoWSe_2$ sheets may be realized from figures 7(e), (f), which resembles *textbook page-like puffy* flakes with dimensions in the micrometer range. The corresponding XRF spectrum in figure S7(b) shows the presence of Mo, W, and Se peaks (elemental composition similar to the neat electrode for the alloy TMD)—the Na and O peaks and traces of Cl and C are mainly attributed to $NaClO_4$ salt in organic electrolyte. Compared to the Na^+ ion half-cells, the K^+ ion disassembled half-cell electrodes showed surface cracks (marked in figure 7(g))—approximately micrometer in dimension (marked in figure 7(h)), with traces of separator fibers on the surface. These surface cracks can be correlated to the strain induced within the $MoWSe_2$ flakes during prolonged cycling. The XRF spectra in figure S7(c) of 0.01–1.5 V cycled K^+ ion half-cells show the Mo, W, and Se elements along with large amounts of K (due to K^+ ion insertion into the material) and traces of electrolyte elements (e.g. P and F arising from the salt, and C arising from the solvent, conducting agent and binder). The lower capacity of K^+ ion half-cells at different voltage ranges in comparison with Na^+ ion half-cells can be well correlated with the higher ionic radius of K^+ ions and the surface cracks visible from the post-cycled electrodes likely originating during repeated potassiation and depotassiation. Overall, the usefulness of the voltage cut-off technique in determining the optimum charge/discharge voltage potentials (for maximum capacity retention for a given class of electrode materials) is further emphasized by post-cycling analysis. The electrodes charged to 2.5 V reveal significant damages in contrast with the electrodes charged to 1.5 V, which maintained the stoichiometry and layered morphology of $MoWSe_2$

even after harsh (high C-rate) and prolonged cycling conditions.

5. Conclusion

This research is the first work to study the Na^+ and K^+ ion storage behavior of cation-substituted $MoWSe_2$ alloy. Because traditional TMDs experience side reactions and significant volume changes that lead to capacity fading and instability during prolonged cycling in LIB, similar or more significant material degradation for long cycling for beyond lithium alkali metal-ions was expected from cation-substituted TMD alloys such as the $MoWSe_2$. Therefore, this study restricted the potential range for charge–discharge to prevent structural disorientation. When cycled at potential ranges of 0.01–2.5 V, the $MoWSe_2$ showed continuous capacity degradation during rate capability and cycling stability tests, indicating structural and chemical degradation, as confirmed by 3D differential capacity surface plots and electron microscopy. Suspension of the potential range to 0.01–2.0 V led to 16% better capacity retention for Na^+ ion half-cells, and additional potential range restriction to 0.01–1.5 V resulted in approx. 29% higher capacity retention than the 2.5 V cycled cell. High coulombic efficiency was observed in the cell with voltage potential range of 0.01–1.5 V, especially in the K^+ ion half-cells. Reaction analysis of the differential curve showed that high upper voltage suspension restricts specific undesirable reactions during sodiation/desodiation or potassiation/depotassiation and therefore helps preserve the crystal structure of the TMD alloy. The intercalation and conversion reaction occurred for the cells cycled within high potential ranges (0.01–2.0 V and 0.01–2.5 V), and crystal structure distortion occurred at the initial cycling stages, leading to capacity fading, shown in the 3D differential capacity curve. Noticeably, the benefits of upper voltage cut-off were more apparent in case of Na^+ ion half-cells in contrast to the K^+ ion half-cells during long term cycling. SEM micrographs of cycled cells with higher voltage cut-off showed smooth geometry retention in the case of Na^+ ion half-cell electrodes and microcracks evolution due to potassiation/depotassiation, which is indirect evidence of strain-induced within. Therefore, this study demonstrated that regulating the operating potential range strongly influences structural preservation, thereby expediting electrochemical performance, specifically cycling stability, capacity retention, and coulombic efficiency of layered $MoWSe_2$. Although full capacity retention from higher voltage cut-off (or cycling within a lower potential range) was not realized, this study nevertheless lays the ground for utilizing the upper voltage cut-off technique combined with composite electrode formation for future investigations regarding the search of next-generation NIB and KIB anodes.

Acknowledgments

This work is supported by the National Science Foundation grants #1743701, 1454151, and 2025298. The research was performed in part in the Nebraska Nanoscale Facility: National Nanotechnology Coordinated Infrastructure and the Nebraska Center for Materials and Nanoscience (and/or NERCF), which are supported by the National Science Foundation under Award ECCS: 2025298, and the Nebraska Research Initiative. The authors also acknowledge the help of Dr Shakir Bin Mujib regarding SEM and XRF experiments for post-cycling analysis.

Data availability statement

The data that support the findings of this study are openly available at the following URL/DOI: https://doi.org/https://ksuemailprod-my.sharepoint.com/:f:/g/personal/sonjoy_ksu_edu/EmYrlUOxm-9EmEljZyVs0WQBWEuYoRqY5KTh3OiSCO_00Q?e=muoT7p.

Author contributions

Conceptualization: GS; methodology: GS and SD; analysis: SD; investigation: SD; resources: GS; data curation: SD; writing—original draft preparation: SD; writing—review and editing: GS; visualization: SD; supervision: GS; funding acquisition: GS. All authors have read and agreed to the published version of the manuscript.

Funding information

This work is supported by the National Science Foundation Grant # 1743701, 1454151, and 2025298.

ORCID iDs

Sonjoy Dey https://orcid.org/0000-0001-6244-2750

References

[1] Wang J, Fan L, Liu Z, Chen S, Zhang Q, Wang L, Yang H, Yu X and Lu B 2019 *In situ* alloying strategy for exceptional potassium ion batteries *ACS Nano* **13** 3703–13
[2] Niu F, Yang J, Wang N, Zhang D, Fan W, Yang J and Qian Y 2017 $MoSe_2$-covered N,P-doped carbon nanosheets as a long-life and high-rate anode material for sodium-ion batteries *Adv. Funct. Mater.* **27** 1700522
[3] Ge J, Fan L, Wang J, Zhang Q, Liu Z, Zhang E, Liu Q, Yu X and Lu B 2018 $MoSe_2$/N-doped carbon as anodes for potassium-ion batteries *Adv. Energy Mater.* **8** 1801477
[4] Sun D, Ye D, Liu P, Tang Y, Guo J, Wang L and Wang H 2018 MoS_2/graphene nanosheets from commercial bulky

MoS_2 and graphite as anode materials for high rate sodium-ion batteries *Adv. Energy Mater.* **8** 1702383
[5] Xu Y, Bahmani F, Zhou M, Li Y, Zhang C, Liang F, Kazemi S H, Kaiser U, Meng G and Lei Y 2019 Enhancing potassium-ion battery performance by defect and interlayer engineering *Nanoscale Horiz.* **4** 202–7
[6] Dong H, Xu Y, Zhang C, Wu Y, Zhou M, Liu L, Dong Y, Fu Q, Wu M and Lei Y 2018 MoS_2 nanosheets with expanded interlayer spacing for enhanced sodium storage *Inorg. Chem. Frontiers* **5** 3099–105
[7] David L, Bhandavat R and Singh G 2014 MoS_2/graphene composite paper for sodium-ion battery electrodes *ACS Nano* **8** 1759–70
[8] Sui R, Zan G, Wen M, Li W, Liu Z, Wu Q and Fu Y 2022 Dual carbon design strategy for anodes of sodium-ion battery: mesoporous CoS2/CoO on open framework carbon-spheres with rGO encapsulating *ACS Appl. Mater. Interfaces* **14** 28004–13
[9] Xu J, Liu Q, Dong Z, Wang L, Xie X, Jiang Y, Wei Z, Gao Y, Zhang Y and Huang K 2021 Interconnected MoS_2 on 2D graphdiyne for reversible sodium storage *ACS Appl. Mater. Interfaces* **13** 54974–80
[10] Lei T, Chen W, Huang J, Yan C, Sun H, Wang C, Zhang W, Li Y and Xiong J 2017 Multi-functional layered WS_2 nanosheets for enhancing the performance of lithium–sulfur batteries *Adv. Energy Mater.* **7** 1601843
[11] Feng C, Huang L, Guo Z and Liu H 2007 Synthesis of tungsten disulfide (WS_2) nanoflakes for lithium ion battery application *Electrochem. Commun.* **9** 119–22
[12] Dey S, Mujib S B and Singh G 2022 Enhanced Li-ion rate capability and stable efficiency enabled by MoSe2 nanosheets in polymer-derived silicon oxycarbide fiber electrodes *Nanomaterials* **12** 553
[13] Li Y, Liang Y, Robles Hernandez F C, Deog Yoo H, An Q and Yao Y 2015 Enhancing sodium-ion battery performance with interlayer-expanded MoS_2–PEO nanocomposites *Nano Energy* **15** 453–61
[14] Ren X, Zhao Q, McCulloch W D and Wu Y 2017 MoS_2 as a long-life host material for potassium ion intercalation *Nano Res.* **10** 1313–21
[15] Mann J *et al* 2014 2-Dimensional transition metal dichalcogenides with tunable direct band gaps: MoS2(1–x) Se2x monolayers *Adv. Mater.* **26** 1399–404
[16] Chen Y, Xi J, Dumcenco D O, Liu Z, Suenaga K, Wang D, Shuai Z, Huang Y-S and Xie L 2013 Tunable band gap photoluminescence from atomically thin transition-metal dichalcogenide alloys *ACS Nano* **7** 4610–6
[17] Tan T L, Ng M-F and Eda G 2016 Stable monolayer transition metal dichalcogenide ordered alloys with tunable electronic properties *J. Phys. Chem.* C **120** 2501–8
[18] Ma X, Wu X, Wang H and Wang Y 2018 A janus MoSSe monolayer: a potential wide solar-spectrum water-splitting photocatalyst with a low carrier recombination rate *J. Mater. Chem.* A **6** 2295–301
[19] Idrees M, Din H U, Ali R, Rehman G, Hussain T, Nguyen C V, Ahmad I and Amin B 2019 Optoelectronic and solar cell applications of Janus monolayers and their van der Waals heterostructures *Phys. Chem. Chem. Phys.* **21** 18612–21
[20] Jin C, Tang X, Tan X, Smith S C, Dai Y and Kou L 2019 A janus MoSSe monolayer: a superior and strain-sensitive gas sensing material *J. Mater. Chem.* A **7** 1099–106
[21] Cai G, Peng L, Ye S, Huang Y, Wang G and Zhang X 2019 Defect-rich $MoS_{2(1-x)}Se_{2x}$ few-layer nanocomposites: a superior anode material for high-performance lithium-ion batteries *J. Mater. Chem.* A **7** 9837–43
[22] Ersan F, Gökoğlu G and Aktürk E 2015 Adsorption and diffusion of lithium on monolayer transition metal dichalcogenides ($MoS_{2(1-x)}Se_{2x}$) alloys *J. Phys. Chem.* C **119** 28648–53
[23] Bhoyate S, Park B, Oh S H and Choi W 2021 Defect engineered MoWS alloy catalyst boost the polysulfide conversion in lithium–sulfur battery *J. Power Sources* **511** 230426
[24] Barik G and Pal S 2018 Monolayer transition-metal dichalcogenide $Mo_{1-x}W_xS_2$ Alloys as efficient anode materials for lithium-ion batteries *J. Phys. Chem.* C **122** 25837–48
[25] Liu B, Liu Y, Hu X, Zhong G, Li J, Yuan J and Wen Z 2021 N-doped carbon modifying MoSSe nanosheets on hollow cubic carbon for high-performance anodes of sodium-based dual-ion batteries *Adv. Funct. Mater.* **31** 2101066
[26] Huang Y, Wang Z, Guan M, Wu F and Chen R 2020 Toward rapid-charging sodium-ion batteries using hybrid-phase molybdenum sulfide selenide-based anodes *Adv. Mater.* **32** 2003534
[27] Kim Y, Kim S, Hong M and Byon H R 2021 Tubular MoSSe/carbon nanotube electrodes for hybrid-ion capacitors *Electrochim. Acta* **374** 137971
[28] Yang C *et al* 2018 Metallic graphene-Like VSe_2 ultrathin nanosheets: superior potassium-ion storage and their working mechanism *Adv. Mater.* **30** 1800036
[29] He H *et al* 2019 Anion vacancies regulating endows mosse with fast and stable potassium ion storage *ACS Nano* **13** 11843–52
[30] Gao Y, Liu K, Wu Y, Li C, Lü Q and Zu G 2023 A strategy of combination reaction to improve electrochemical performance in two-dimensional $Mo_{1-x}W_xSe_2$ battery-type electrode materials *Ceram. Int.* **49** 7196–207
[31] Ghosh S, Qi Z, Wang H, Martha S K and Pol V G 2021 WS2 anode in Na and K-ion battery: Effect of upper cut-off potential on electrochemical performance *Electrochim. Acta* **383** 138339
[32] Dong Y, Xu Y, Li W, Fu Q, Wu M, Manske E, Kröger J and Lei Y 2019 Insights into the crystallinity of layer-structured transition metal dichalcogenides on potassium ion battery performance: a case study of molybdenum disulfide *Small* **15** 1900497
[33] Patel A B, Machhi H K, Chauhan P, Narayan S, Dixit V, Soni S S, Jha P K, Solanki G K, Patel K D and Pathak V M 2019 Electrophoretically deposited $MoSe_2$/WSe_2 heterojunction from ultrasonically exfoliated nanocrystals for enhanced electrochemical photoresponse *ACS Appl. Mater. Interfaces* **11** 4093–102
[34] Zhang S, Wang G, Jin J, Zhang L, Wen Z and Yang J 2018 Robust and conductive red $MoSe_2$ for stable and fast lithium storage *ACS Nano* **12** 4010–8
[35] Bai J, Zhang L, Li S, Ren H, Liu Y and Guo S 2023 Self-assembled $MoTe_2$ hierarchical nanoflowers with carbon coating as anode material for excellent sodium storage performance *Chem. Eng. J.* **452** 139111
[36] Sierra-Castillo A, Haye E, Acosta S, Bittencourt C and Colomer J F 2020 Synthesis and characterization of highly crystalline vertically aligned WSe2 nanosheets *Appl. Sci.* **10** 874
[37] Liang F, Xu H, Wu X, Wang C, Luo C and Zhang J 2018 Raman spectroscopy characterization of two-dimensional materials* *Chin. Phys.* B **27** 037802
[38] Jiang Q, Lu Y, Huang Z and Hu J 2017 Facile solvent-thermal synthesis of ultrathin $MoSe_2$ nanosheets for hydrogen evolution and organic dyes adsorption *Appl. Surf. Sci.* **402** 277–85
[39] Zhang M *et al* 2014 Two-dimensional molybdenum tungsten diselenide alloys: photoluminescence, raman scattering, and electrical transport *ACS Nano* **8** 7130–7

[40] Wang H, Kong D, Johanes P, Cha J J, Zheng G, Yan K, Liu N and Cui Y 2013 $MoSe_2$ and WSe_2 nanofilms with vertically aligned molecular layers on curved and rough surfaces *Nano Lett.* **13** 3426–33
[41] Late D J, Shirodkar S N, Waghmare U V, Dravid V P and Rao C N R 2014 Thermal expansion, anharmonicity and temperature-dependent raman spectra of single- and Few-Layer $MoSe_2$ and WSe_2 *ChemPhysChem* **15** 1592–8
[42] Barough V, Iranizad E S, Bayat A and Hemmati K 2018 Synthesis of binder-free $MoSe_2$ nanoflakes as a new electrode for electrocatalytic hydrogen evolution *J. Electroanal. Chem.* **823** 278–86
[43] Ahmad H, Reduan S A, Aidit S N, Yusoff N, Maah M J, Ismail M F and Tiu Z C 2019 Ternary $MoWSe_2$ alloy saturable absorber for passively Q-switched Yb-, Er- and Tm-doped fiber laser *Opt. Commun.* **437** 355–62
[44] Terrones H *et al* 2014 New first order raman-active modes in few layered transition metal dichalcogenides *Sci. Rep.* **4** 4215
[45] Luo X, Zhao Y, Zhang J, Toh M, Kloc C, Xiong Q and Quek S Y 2013 Effects of lower symmetry and dimensionality on Raman spectra in two-dimensional WSe ${}_{2}$ *Phys. Rev. B* **88** 7195313
[46] Seifert G, Finster J and Müller H 1980 SW Xα calculations and x-ray photoelectron spectra of molybdenum(II) chloride cluster compounds *Chem. Phys. Lett.* **75** 373–7
[47] Brox B and Olefjord I 1988 ESCA Studies of MoO_2 and MoO_3 *Surf. Interface Anal.* **13** 3–6
[48] Grim S O and Matienzo L J 1975 X-ray photoelectron spectroscopy of inorganic and organometallic compounds of molybdenum *Inorg. Chem.* **14** 1014–8
[49] Kojima I and Kurahashi M 1987 Application of asymmetrical Gaussian/Lorentzian mixed function for x-ray photoelectron curve synthesis *J. Electron. Spectrosc. Relat. Phenom.* **42** 177–81
[50] Xie X and McCarley R E 1995 Synthesis, structure, and characterization of N-ligated tungsten selenide cluster complexes W6Se8L6 *Inorg. Chem.* **34** 6124–9
[51] Najafi L, Bellani S, Oropesa-Nuñez R, Ansaldo A, Prato M, Del Rio Castillo A E and Bonaccorso F 2018 Engineered MoSe2-based heterostructures for efficient electrochemical hydrogen evolution reaction *Adv. Energy Mater.* **8** 1703212
[52] Salitra G, Hodes G, Klein E and Tenne R 1994 Highly oriented WSe_2 thin films prepared by selenization of evaporated WO3 *Thin Solid Films* **245** 180–5
[53] Zhang Z, Yang X and Fu Y 2016 Nanostructured WSe2/C composites as anode materials for sodium-ion batteries *RSC Adv.* **6** 12726–9
[54] Cho J S, Park S-K, Jeon K M, Piao Y and Kang Y C 2018 Mesoporous reduced graphene oxide/WSe2 composite particles for efficient sodium-ion batteries and hydrogen evolution reactions *Appl. Surf. Sci.* **459** 309–17
[55] Share K, Lewis J, Oakes L, Carter R E, Cohn A P and Pint C L 2015 Tungsten diselenide (WSe2) as a high capacity, low overpotential conversion electrode for sodium ion batteries *RSC Adv.* **5** 101262–7
[56] Hoe Seon Y, Chan Kang Y and Cho J S 2021 One-dimensional porous nanostructure composed of few-layered MoSe2 nanosheets and highly densified-entangled-N-doped CNTs as anodes for Na ion batteries *Chem. Eng. J.* **425** 129051
[57] Fly A and Chen R 2020 Rate dependency of incremental capacity analysis (dQ/dV) as a diagnostic tool for lithium-ion batteries *J. Energy Storage* **29** 101329
[58] Pan H, Lu X, Yu X, Hu Y-S, Li H, Yang X-Q and Chen L 2013 Sodium Storage and Transport Properties in Layered Na2Ti3O7 for Room-Temperature Sodium-Ion Batteries *Adv. Energy Mater.* **3** 1186–94
[59] Jiao X, Liu X, Wang B, Wang G, Wang X and Wang H 2020 A controllable strategy for the self-assembly of WM nanocrystals/nitrogen-doped porous carbon superstructures (M = O, C, P, S, and Se) for sodium and potassium storage *J. Mater. Chem.* A **8** 2047–65
[60] Chen X, Muheiyati H, Sun X, Zhou P, Wang P, Ding X, Qian Y and Xu L 2022 Rational design of tungsten selenide @ N-doped carbon nanotube for high-stable potassium-ion batteries *Small* **18** 2104363
[61] Ge P, Hou H, Banks C E, Foster C W, Li S, Zhang Y, He J, Zhang C and Ji X 2018 Binding $MoSe_2$ with carbon constrained in carbonous nanosphere towards high-capacity and ultrafast Li/Na-ion storage *Energy Storage Mater.* **12** 310–23
[62] Oh H G and Park S-K 2022 Co-MOF derived $MoSe_2$@$CoSe_2$/N-doped carbon nanorods as high-performance anode materials for potassium ion batteries *Int. J. Energy Res.* **46** 10677–88
[63] Yun Q, Li L, Hu Z, Lu Q, Chen B and Zhang H 2020 Layered transition metal dichalcogenide-based nanomaterials for electrochemical energy storage *Adv. Mater.* **32** 1903826
[64] Regulacio M D, Nguyen D-T, Horia R and Seh Z W 2021 Designing nanostructured metal chalcogenides as cathode materials for rechargeable magnesium batteries *Small* **17** 2007683
[65] Soares D M, Mukherjee S and Singh G 2020 TMDs beyond MoS_2 for electrochemical energy storage *Chem.—A Eur. J.* **26** 6320–41